Electrokinetic instability due to streamwise conductivity gradients in microchip electrophoresis

Kaushlendra Dubey[1], Sanjeev Sanghi[2], Amit Gupta[1] and Supreet Singh Bahga[1],†

[1]Department of Mechanical Engineering, Indian Institute of Technology Delhi, New Delhi, 110016, India
[2]Department of Applied Mechanics, Indian Institute of Technology Delhi, New Delhi, 110016, India

We present an experimental and numerical investigation of electrokinetic instability (EKI) in microchannel flow with streamwise conductivity gradients, such as those observed during sample stacking in capillary electrophoresis. A plug of a low-conductivity electrolyte solution is initially sandwiched between two high-conductivity zones in a microchannel. This spatial conductivity gradient is subjected to an external electric field applied along the microchannel axis, and for sufficiently strong electric fields an instability sets in. We have explored the physics of this EKI through experiments and numerical simulations, and supplemented the results using scaling analysis. We performed EKI experiments at different electric field values and visualised the flow using a passive fluorescent tracer. The experimental data were analysed using the proper orthogonal decomposition technique to obtain a quantitative measure of the threshold electric field for the onset of instability, along with the corresponding coherent structures. To elucidate the physical mechanism underlying the instability, we performed high-resolution numerical simulations of ion transport coupled with fluid flow driven by the electric body force. Simulations reveal that the non-uniform electroosmotic flow due to axially varying conductivity field causes a recirculating flow within the low-conductivity region, and creates a new configuration wherein the local conductivity gradients are orthogonal to the applied electric field. This configuration leads to EKI above a threshold electric field. The spatial features of the instability predicted by the simulations and the threshold electric field are in good agreement with the experimental observations and provide useful insight into the underlying mechanism of instability.

Key words: electrokinetic flows, microfluidics

† Email address for correspondence: bahga@mech.iitd.ac.in

1. Introduction

The advent of microfluidic devices has led to the development of microchip electrophoresis systems which enable rapid separation and detection of charged species from a small volume of sample mixture (Jacobson & Ramsey 1995). Electrophoresis techniques are characterised by electrophoretic motion of ions and advection due to interfacially driven electroosmotic flow (EOF) (Levich 1962) past the charged surface of the microchannel in the presence of an electric field. Microchip electrophoresis is often performed by incorporating a sample-stacking step wherein the sample mixed with low electrical conductivity electrolyte is introduced between two zones of high-conductivity electrolyte (Jacobson & Ramsey 1995). The gradient in the local electric field associated with the conductivity gradient causes the sample ions to stack at the boundary of high- and low-conductivity zones prior to the separation, thereby improving the detection sensitivity (Bharadwaj & Santiago 2005; Dubey, Gupta & Bahga 2019).

A typical configuration of high- and low-conductivity electrolytes that is used for sample stacking in electrophoresis is illustrated in figure 1. Initially, a low-conductivity electrolyte is sandwiched between two zones of a high-conductivity electrolyte inside a microchannel, typically fabricated in glass. The high- and low-conductivity electrolytes are made by varying the acid and base concentrations in water. A strong external electric field is applied along the channel axis. The continuity of current in the channel results in the local electric field being higher and lower in the low- and high-conductivity regions, respectively. The axially varying electric field drives a fluid flow through two distinct mechanisms. Firstly, the axially varying electric field induces a non-uniform electroosmotic slip velocity at the channel walls due to the presence of immobile surface charges on the walls. In the absence of conductivity gradients, the bulk EOF driven by this electroosmotic slip velocity has a plug-shaped velocity profile (Levich 1962). However, in the presence of streamwise conductivity gradients, the slip velocity is higher in the regions with low conductivity and lower in the high-conductivity regions, as depicted in figure 1. The non-uniform electroosmotic slip velocity induces internal pressure gradients to ensure continuity of flow and drives a recirculating flow over a mean flow that advects the conductivity field along the channel axis. The EOF driven by an inhomogeneous slip velocity at the channel walls (Anderson & Idol 1985; Ajdari 1995) and its detrimental effects on electrophoretic separations due to sample dispersion have been studied extensively (Keely, van de Goor & McManigill 1994; Herr *et al.* 2000; Sounart & Baygents 2001).

Besides the interfacially driven EOF, the gradients in the local electric field accompanied by conductivity gradients can lead to instabilities in the flow (Hoburg & Melcher 1977; Baygents & Baldessari 1998; El Moctar, Aubry & Batton 2003; Chen *et al.* 2005; Posner & Santiago 2006; Gaur & Bahga 2017; Sharan, Gupta & Bahga 2017). The electric field gradients lead to accumulation of free charge within the bulk fluid. In turn, this free charge couples with the local electric field to apply a destabilising electric body force on the fluid, which has the capability to induce an electrohydrodynamic instability. When such an instability appears in systems along with EOF, where EOF drives the fluid flow, the resulting instability is often termed an electrokinetic instability (EKI) (Chen *et al.* 2005; Ramos 2011). In microfluidic applications where significant mixing of fluids is desired, EKI is used as an active method for rapid mixing (Oddy, Santiago & Mikkelsen 2001; Lin *et al.* 2004; Dubey, Gupta & Bahga 2017). On the other hand, in microchip electrophoresis, such instabilities are undesirable as they can lead to the rapid dispersion of sample ions and deteriorate the separation performance (Ramsey 2001; Lin 2009).
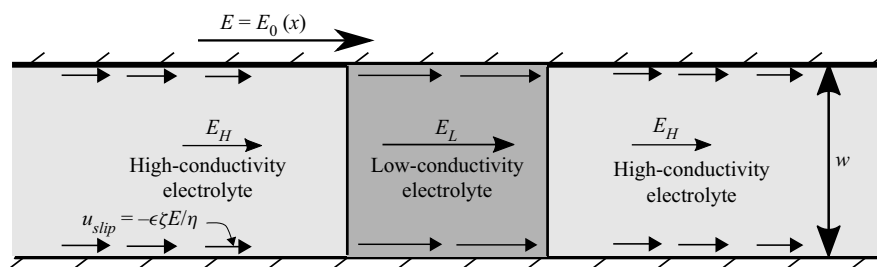
Figure 1. Schematic illustrating typical conductivity distribution required for sample-stacking step in microchip electrophoresis. Initially, a plug of low-conductivity electrolyte is surrounded by two high-conductivity electrolyte zones. An external electric field is applied along the axial direction. The axial gradients in conductivity lead to corresponding variations in the local electric field and the local electroosmotic slip velocity at the channel walls. The non-uniform electroosmotic slip velocity results in internal pressure gradients which lead to a non-uniform EOF.

Electrokinetic instabilities have been investigated experimentally and theoretically in various microchannel flow configurations, primarily for rapid mixing in low Reynolds number flows (Chen *et al.* 2005; Lin, Storey & Santiago 2008; Luo 2009; Posner, Pérez & Santiago 2012; Demekhin, Nikitin & Shelistov 2013, 2014; Dubey *et al.* 2017). However, EKI during sample stacking in electrophoresis (figure 1) is still not well characterised. Various studies of sample stacking in microchip electrophoresis have reported that large conductivity gradients in the presence of a strong electric field deteriorate the separation efficiency possibly due to EKI (Shultz-Lockyear *et al.* 1999; Dang *et al.* 2003). The only conclusive report on EKI during sample stacking in microchip electrophoresis is that by Santos & Storey (2008), who performed numerical simulations of flow in a configuration similar to that shown in figure 1. Through simulations, Santos & Storey (2008) predicted recirculating flow in a frame of reference moving with the mean flow and the onset of instability above a threshold electric field. However, direct empirical evidence of the existence of such EKI has still not been reported. The key challenges in experimentally observing the EKI during sample stacking are the diffusive nature of the conductivity gradient, illustrated in figure 1, and the short time scale associated with EKI (Santos & Storey 2008).

This paper presents a detailed experimental and numerical investigation of the EKI that occurs when a strong electric field is applied across a streamwise conductivity gradient in a microchannel, such as that during sample stacking in electrophoresis. We performed a series of controlled experiments involving high-speed imaging of a passive scalar for various electric field values to visualise this instability. Based on the analysis of experimental data, we report the dominant flow structures and the threshold criteria for the onset of instability. We supplement our empirical observations with numerical simulations to elucidate the physical mechanism underlying this instability. The experimental observations and simulation predictions clearly show that the instability results from the coupling of the electric field and the conductivity gradients set up by the non-uniform EOF.

The paper is structured as follows. Section 2 presents the experimental set-up and data analysis techniques. Section 3 presents the experimental observations. Sections 4 and 5 present the simulation approach and description of the physical mechanism of the instability through simulation results. The paper is then concluded in § 6 with remarks on the implications of the experimental and simulation results.
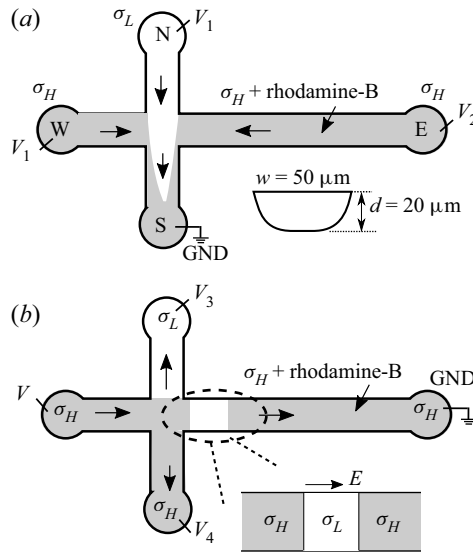
Figure 2. Schematic illustrating the two-step procedure of experiment to visualise the EKI in a cross-shaped microchip. First, conductivity gradients are established by introducing a low-conductivity electrolyte from the north reservoir of the microchip and high-conductivity electrolytes from the east and west reservoirs. The electrolytes flow in the direction of the electric field in the respective channels. The flow is visualised by mixing Rhodamine-B dye with the high-conductivity electrolyte present in the east channel. Thereafter, upon switching the voltages at the reservoirs, the electric field in the main channel becomes colinear with the conductivity gradients. All the microchannels have a D-shaped cross-section with channel width w and depth d.

2. Experiments

2.1. *Description of the flow*

We performed experiments to visualise the EKI that sets in when a strong electric field is applied across a fluid in a microchannel with a streamwise gradient in electrical conductivity, as shown in figure 1. The schematic shown in figure 2 illustrates the two-step procedure that was devised to perform the experiments in a cross-shaped microchip. Figure 2(*a*) shows the injection step, wherein a low-conductivity (σ_L) electrolyte is filled in the north (N) reservoir and a high-conductivity electrolyte (σ_H) is filled in the west (W), east (E) and south (S) reservoirs. An electrically neutral fluorescent tracer, Rhodamine-B, is mixed in the high-conductivity electrolyte filled in the E channel to visualise the flow during experiments. In the first step, electric potential V_1 is applied at N and W reservoirs, and potential $V_2 > V_1$ is applied at the E reservoir. This results in an EOF from the E, W and N reservoirs towards the cross-junction. The incoming fluid streams at the cross-junction flow towards the S reservoir, which serves as the sink. This flow configuration results in hydrodynamic focusing of the low-conductivity stream between two high-conductivity streams at the channel junction. The steady-state hydrodynamic focusing is achieved within one minute. Once a steady flow is achieved during the injection step, the interfaces between high- and low-conductivity zones in the main channel remain stationary at the cross-junction. This steady flow configuration results in a narrow plug of the low-conductivity electrolyte sandwiched between two adjacent zones of high-conductivity electrolytes. In the next step, the potentials at the channel ends are suddenly switched to generate an electric field that is collinear with the conductivity gradient, as shown in figure 2(*b*). Consequently, the EOF advects the low-conductivity plug

Symbol	Description	Value
ϵ	Permittivity of water	6.93×10^{-10} C V^{-1} m^{-1}
D_+	Diffusivity of sodium ion	13.3×10^{-10} m^2 s^{-1}
D_-	Diffusivity of MOPS ion	6.9×10^{-10} m^2 s^{-1}
η	Dynamic viscosity of water	1×10^{-3} kg m s^{-1}
ζ	Zeta-potential	-7.47×10^{-2} V
ρ	Density of water	1×10^3 kg m^{-3}
γ	Conductivity ratio (σ_H/σ_L)	10
w	Channel width	50×10^{-6} m
d	Channel depth	20×10^{-6} m

Table 1. Properties of the electrolyte solutions and physical parameters of the microfluidic device.

into the main channel, connecting the cross-junction and the E reservoir. This results in a configuration similar to that depicted in figure 1. For the second step, the potentials applied at the N and S reservoirs are chosen so that the EOF in the vertical channels is minimised. No external pressure is applied at the channel ends, and all the reservoirs were maintained at atmospheric pressure. We tried various ways of visualising the flow by mixing the passive fluorescent tracer in other zones. As described later in § 4, the instability dynamics is primarily governed by the leading interface, due to which mixing the tracer in the leading high-conductivity zone provides the best visualisation of the instability.

2.2. *Electrolyte solutions*

The high- and low-conductivity electrolyte solutions were prepared upon diluting the stock solutions of 1 M each of MOPS (Sigma Aldrich, USA) and NaOH (CDH, India) using deionised water. The electrolyte having high conductivity consisted of 200 mM MOPS and 125 mM NaOH (pH = 7.3). The measured electrical conductivity of the high-conductivity electrolyte was $\sigma_H = 0.51$ S m^{-1}. The low-conductivity electrolyte consisted of 20 mM MOPS and 10 mM NaOH ($\sigma_L = 0.051$ S m^{-1}, pH = 6.9). The measured conductivity ratio ($\gamma = \sigma_H/\sigma_L$) of these two electrolytes was 10. The viscosity and the permittivity of the electrolytes are assumed to be same as those of pure water due to the low concentration of electrolytes (Horvath 1985). To visualise the conductivity field in our experiments, the electrolyte solution with high conductivity was seeded with 0.5 mM Rhodamine-B which is reported to be electrically neutral for the pH values of the solution used in the experiments (Milanova *et al.* 2011, 2012). Because a neutral marker has negligible electrophoretic mobility, it does not interact with background electrolytes during the experiments. The values of various physical properties of the electrolyte are provided in table 1.

2.3. *Experimental set-up and image acquisition*

All the experiments were conducted in a standard cross-shaped glass microchip (Micronit, The Netherlands) shown schematically in figure 2. The microchannels connecting the N, W and S reservoirs to the junction were 5 mm long, and the channel connecting the junction to the E reservoir was 35 mm long. All the channels had a D-shaped cross-section of width $w = 50$ µm and depth $d = 20$ µm. Large reservoirs were attached to the channel ends to minimise variability due to evaporation, buffer depletion and unwanted pressure-driven flow due to the change in liquid level in the reservoirs during the experiments.

A four-channel high voltage power supply (IONICS, India, max. 2 kV and 10 mA) was used to apply potential difference across the channels. Platinum wires were used as electrodes dipped into the reservoirs. The electric field direction in the channels was controlled by switching the electric potential at each reservoir using a computer-controlled relay switch. To visualise the scalar field, we used an inverted epifluorescence microscope (Nikon Eclipse Ti-U, Japan) equipped with a mercury arc lamp, $\times$ 20 objective (Plan Fluor, ELWD, NA = 0.45), and Nikon G2-A filter set (510–560 nm bandpass excitation filter, 590 nm longpass barrier filter). The spatio-temporal evolution of the scalar concentration field was recorded using a Peltier-cooled high-speed sCMOS camera (Andor Zyla 5.5, UK).

For all the experiments, the image acquisition was started 1 s before applying the electric field to capture all the phases of the experiment. We acquired images of size 2560×150 pixels which corresponds to 985×58 µm physical area of the microfluidic chip. These snapshots were recorded at 572 f.p.s. for each experiment with an exposure of 1 ms. The data were also acquired at high frame rates of 650 and 850 f.p.s. and had similar spectral content, indicating the absence of aliasing.

Each snapshot of the scalar concentration field was corrected using a standard image correction method,

$$I(x, y)_{corrected} = \frac{I(x, y)_{raw} - \overline{I(x, y)_{bg}}}{\overline{I(x, y)_{ff}} - \overline{I(x, y)_{bg}}}, \tag{2.1}$$

$$\text{where} \quad \overline{I(x, y)} = \frac{\sum\limits_{1}^{N} I(x, y)}{N}. \tag{2.2}$$

Here, I_{raw}, I_{ff} and I_{bg} denote the raw, flat field and the background snapshots, respectively. The flat field images were obtained by filling all the channels uniformly with the electrolyte solution mixed with the fluorescent dye, whereas background images were captured by filling the electrolyte solution without the dye. This normalisation of pixel intensity was used to correct the raw signal for non-uniformity arising due to non-uniform illumination and the D-shape of the channel cross-section.

2.4. *Experimental conditions*

We conducted the experiments for six different electric field values in the range $E = 10$–60 kV m^{-1} while keeping the ratio of conductivity of electrolytes fixed at $\sigma_H/\sigma_L = 10$. These values of the electric field are typical of those used in practical microchip sample stacking, which can vary between 10 and 100 kV m^{-1} (Jacobson & Ramsey 1995; Bharadwaj & Santiago 2005). The experiments were performed with an increment of $\Delta E = 10$ kV m^{-1} from an initial low electric field at which the flow is stable. In our work, we define the electric field as $E = (V_W - V_E)/L$, where V_E and V_W denote the potentials at E and W reservoirs, respectively, and $L = (L_E + L_W)$ denotes the sum of E and W channel lengths. Three repetitions of each experiment were performed on the same microfluidic chip to ensure repeatability of the phenomena. For the initial step of the experiment, shown in figure 2(*a*), we kept the same initial values of electric potentials ($V_1 = 0.75$ kV and $V_2 = 1.45$ kV) at various reservoirs for all the experiments.

Before each experiment, all the microchannels were flushed sequentially with a 100 mM sodium hydroxide solution for 10 min and then using deionised water for another 10 min.

After cleaning the microfluidic device, a fixed volume of 25 µl of each electrolyte solution was filled in the respective reservoirs and vacuum was applied momentarily at S reservoir to fill all the channels. Subsequently, the electric potential was applied at various reservoirs to initiate the first step of hydrodynamically focusing the low-conductivity stream between two high-conductivity streams. We waited for over one minute to achieve steady hydrodynamic injection. Finally, at $t = 0$, the electric potential at each reservoir was switched in such a way that the low-conductivity zone moved further into the E channel, creating the configuration of collinear electric field and conductivity gradient, as shown in figure 2(*b*). Hence, at the beginning of the second step, at $t = 0$, the low-conductivity plug is at the channel junction. Later during the second step, the plug advects downstream of the E channel due to EOF.

2.5. *Time scales and dimensionless numbers*

The conductivity field in our experiments evolves due to advection and diffusion of electrolyte ions. Diffusion has a stabilising effect on the flow as it tends to diminish the conductivity gradients responsible for the instability. The time scale corresponding to the diffusion of the conductivity field is given by

$$\tau_{diff} \equiv \frac{w^2}{D_{eff}}, \quad \text{where } D_{eff} = \frac{2D_+ D_-}{D_+ + D_-}. \tag{2.3}$$

Here, D_{eff} is the effective diffusivity of the conductivity field (see § 4.1), $D_{\pm}$ denote the diffusivities of cations and anions of the electrolyte and w is the width of the microchannel.

The fluid flow in the microchannel is driven by the electroosmotic slip at the channel walls with immobile surface charges and an electric body force that arises when an electric field is applied across a conductivity gradient. The electroosmotic slip velocity depends on the local tangential electric field E_t as (Hunter 1981; Probstein 2005)

$$u_{eof} = -\frac{\epsilon \zeta E_t}{\eta} = \mu_{eof} E_t, \tag{2.4}$$

where $\mu_{eof} = -\epsilon \zeta / \eta$ is termed the electroosmotic mobility of the channel surface. Here, ϵ is the permittivity of electrolyte, η the dynamic viscosity and ζ the zeta-potential at the channel surface. For the system that we have considered in the current work, most of the main channel is filled with the high-conductivity electrolyte, as shown in figure 2(*b*). Therefore, the mean EOF velocity in the channel scales as $\mu_{eof} E$, where $E = (V_W - V_E)/(L_W + L_E)$ is the reference scale for the mean electric field in the channel. The corresponding time scale for advection due to EOF is given by

$$\tau_{eof} \equiv \frac{w}{\mu_{eof} E}. \tag{2.5}$$

The instability is driven by an electric body force on the fluid that results from the coupling of electric field with the free charge in the regions with conductivity gradient. The appropriate reference scale for the resulting velocity, termed the electroviscous velocity U_{ev}, is obtained by balancing the viscous and the electric body forces, $\eta \nabla^2 \boldsymbol{u} \sim \rho_f \boldsymbol{E}$, where $\boldsymbol{u}$ denotes the velocity, ρ_f the free charge density and $\boldsymbol{E}$ the local electric field. As shown by Hoburg & Melcher (1976), from the continuity of current and Gauss's law, the free charge density is given by $\rho_f = \epsilon \boldsymbol{\nabla} \cdot \boldsymbol{E} = -\epsilon \boldsymbol{E} \cdot \boldsymbol{\nabla} \sigma / \sigma$ (see § 4.1). By balancing the viscous and

the electric body forces, we arrive at the electroviscous velocity U_{ev} and time scale τ_{ev},

$$U_{ev} \equiv \frac{\epsilon E^2 w}{\eta} \quad \text{and} \quad \tau_{ev} \equiv \frac{w}{U_{ev}} = \frac{\eta}{\epsilon E^2}. \tag{2.6a,b}$$

Based on the values of various physical parameters of the electrolyte solutions and the microfluidic device given in table 1 and for a typical value of electric field $E = 30\,\text{kV m}^{-1}$, the typical values of various time scales of the problem are: $\tau_{diff} = 2.75\,\text{s}$, $\tau_{eof} = 32\,\text{ms}$ and $\tau_{ev} = 1.6\,\text{ms}$. For these experimental conditions, the time scale corresponding to the destabilising electroviscous velocity (τ_{ev}) is significantly smaller than the time scale for diffusion (τ_{diff}) which tends to stabilise the flow. Therefore, one can expect to observe an instability for these experimental conditions.

Besides the three time scales, (τ_{diff}, τ_{eof} and τ_{ev}), the fluid flow in our experiments is governed by the geometric parameters of the device, (w and d), and the conductivity ratio (γ). These six physical parameters can be grouped into the following four dimensionless numbers:

$$Ra_e \equiv \frac{\tau_{diff}}{\tau_{ev}} = \frac{\epsilon E^2 w^2}{\eta D_{eff}}, \quad \frac{(\tau_{ev}\tau_{diff})^{1/2}}{\tau_{eof}} = \frac{-\zeta}{\sqrt{\eta D_{eff}/\epsilon}}, \quad \frac{d}{w} \quad \text{and} \quad \gamma. \tag{2.7a–d}$$

The dimensionless number Ra_e, which is the ratio of time scales associated with diffusion and electrosviscous flow, is called the electric Rayleigh number (Chen *et al.* 2005; Posner & Santiago 2006; Dubey *et al.* 2017) which governs the onset of instability. In electrokinetic systems, the instability sets in at high Ra_e, when electroviscous flow amplifies the disturbances in the conductivity field faster than the rate at which diffusion dissipates these disturbances (Chen *et al.* 2005; Posner & Santiago 2006; Dubey *et al.* 2017). The second dimensionless number in (2.7a–d) can be interpreted as the dimensionless zeta-potential $-\zeta/\sqrt{\eta D_{eff}/\epsilon}$, which governs the ability of flow perturbations to convect with EOF against the dissipative effects (Chen *et al.* 2005). In the current work, we analyse the stability of electrokinetic flow by varying the electric field and hence the electric Rayleigh number. All other dimensionless numbers are kept constant in our experiments.

3. Experimental results

In this section, we present the features of the instability observed during the fluid flow. Experiments were performed to investigate the stable, onset of instability and unstable flow regimes by varying the electric field and correspondingly the electric Rayleigh number Ra_e, which was calculated based on (2.7a–d) using the physical parameters listed in table 1. For these parameters, the conversion between electric field and Rayleigh number is $E = 0.724\sqrt{Ra_e}$ where the electric field is in kV m^{-1}. In figure 3, we present the time-resolved snapshots of the passive fluorescent tracer in the flow for $Ra_e = 760$, 4770 and 6870.

3.1. *Stable flow*

The evolution of flow at a low electric field value corresponding to $Ra_e = 760$ is shown in figure 3(*a*). The region with conductivity gradients is comparatively small compared with the dimensions of the main channel. Therefore, here we present snapshots of a small region of 150 μm length and 50 μm width. Figure 3(*a*) shows the representative snapshots obtained at different time instants during the experiments. Note that the passive
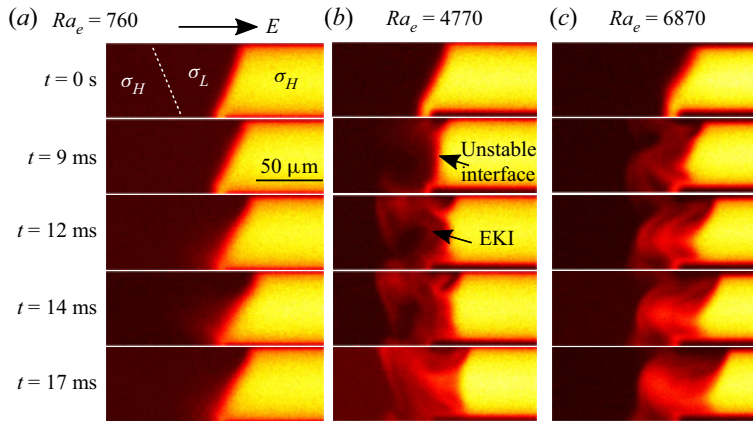
Figure 3. Instantaneous scalar concentration field recorded during experiments at three different electric Rayleigh numbers (Ra_e). All the experiments have the same initial condition, wherein a low-conductivity zone is sandwiched between two high-conductivity zones. At $t = 0$, the voltages at the reservoirs are switched and the electric field in the main channel becomes colinear with the conductivity gradients. The low-conductivity plug is at the channel junction at $t = 0$, and later it advects downstream due to EOF. (a) The flow is stable at low electric field corresponding to $Ra_e = 760$. (b) At a higher electric field, corresponding to $Ra_e = 4770$, an instability is observed. In particular, the high-conductivity electrolyte (dyed with fluorescent tracer) is drawn into the low-conductivity zone in the form of a narrow, oscillating stream. (c) At $Ra_e = 6870$, the growth of instability is even faster. The instability at $Ra_e = 4770$ and 6870 is characterised by rapid dispersion of the conductivity gradient.

fluorescent tracer is purposely mixed in the high conductivity stream present on the right-hand side in the E channel to visualise the leading interface separating the high- and low-conductivity zones. Initially, a low-conductivity electrolyte plug is hydrodynamically focused between two high-conductivity streams at the channel junction, which results in a slanted conductivity interface at time $t = 0$. For $Ra_e = 760$, the flow remains stable, and no perturbations in the concentration field of the passive scalar are observed. In figure 3(a), the interface separating the high- and low-conductivity regions on the right, as visualised by the passive scalar, can be seen advecting marginally downstream in the E channel due to EOF. Because the time scale over which the images were acquired was an order of magnitude smaller than the diffusion time scale ($\tau_{diff} = 2.75$ s), the conductivity gradient appears minimally diffused.

3.2. *Unstable flow*

A stable flow is observed in the experiments for electric Rayleigh numbers up to $Ra_e = 1720$. Upon increasing Ra_e, the perturbations in the conductivity field, associated with the EKI, appear within the low-conductivity zone. To show the characteristics of the instability, we present the instantaneous snapshots of scalar concentration field at $Ra_e = 4770$ and 6870, respectively in figure 3(b,c). The snapshots at $t = 0$ are similar for all the experiments performed at different Ra_e as the initial conditions are kept the same. For $Ra_e = 4770$, figure 3(b) shows that the high-conductivity electrolyte seeded with the fluorescent tracer is drawn into the low-conductivity zone in the form of a thin stream. The high-conductivity stream oscillates in the spanwise direction and results in a rapid mixing within the low-conductivity region. Due to the instability, the dispersion of conductivity gradient occurs within ∼10 ms as opposed to the diffusion time scale of $\tau_{diff} \sim 2.75$ s.

As shown in figure 3(*c*), the instability sets in even earlier at higher $Ra_e = 6870$. The features of the instability appear similar to that at $Ra_e = 4770$. The spanwise oscillations of the high-conductivity stream drawn into the low-conductivity region along with the advection of the conductivity gradient due to EOF result in alternating sequences of high- and low-conductivity zones (see figure 3*c* at $t = 12$ ms). Due to the faster growth of instability at $Ra_e = 6870$, the mixing of high- and low-conductivity streams is more uniform than that at $Ra_e = 4770$. The instability fades away at a later time when the conductivity gradient disperses due to rapid mixing.

3.3. *Proper orthogonal decomposition of experimental data*

The instantaneous snapshots presented in figure 3 show that EKI in our experiments occurs for a short time duration before it fades away due to rapid dispersion of the conductivity gradients. We analysed the time-resolved snapshots of scalar concentration field using the proper orthogonal decomposition (POD) technique (Sirovich 1987) to obtain the critical value of Ra_e for the onset of instability and to identify the dominant flow structures. The POD represents the spatio-temporal variation of any physical quantity $v(\boldsymbol{x}, t)$ by a linear combination of spatially orthogonal modes $\psi_i(\boldsymbol{x})$ modulated by the time-dependent coefficients $a_i(t)$ as (Sirovich 1987),

$$v(\boldsymbol{x}, t) = \sum_{i=1}^{\infty} a_i(t) \psi_i(\boldsymbol{x}). \tag{3.1}$$

The spatial modes $\psi_i(\boldsymbol{x})$ form an optimal basis, and they represent the coherent structures present in the flow.

We used the method of snapshots (Sirovich 1987) to compute the POD of the scalar concentration field in our experiments. In this method, the time-resolved snapshots of the scalar field at every time instant are cast in the form for a vector $\boldsymbol{v}_i$ and the data are represented in the form of a matrix $\boldsymbol{V}$ as,

$$\boldsymbol{V} = [\boldsymbol{v}_1, \boldsymbol{v}_2, \boldsymbol{v}_2, \ldots, \boldsymbol{v}_N], \tag{3.2}$$

where N denotes the total number of snapshots. The singular value decomposition of matrix $\boldsymbol{V}$,

$$\boldsymbol{V} = \boldsymbol{U} \boldsymbol{\Sigma} \boldsymbol{W}^T, \tag{3.3}$$

yields the POD of the data acquired at discrete time instants. The matrix $\boldsymbol{U}$ contains the orthogonal modes $\psi_i(\boldsymbol{x})$, whereas the matrix $\boldsymbol{W}$ contains the time coefficients $a_i(t)$ of each mode. The diagonal elements of the diagonal matrix $\boldsymbol{\Sigma}$ are non-negative numbers λ_i, called the singular values, and are arranged in a descending order

$$\lambda^{(1)} \geq \lambda^{(2)} \geq, \ldots, \lambda^{(i)} \geq 0. \tag{3.4}$$

The amount of energy in the signal related to a given POD mode is directly proportional to the corresponding eigenvalue (Fukunaga 1990). Therefore, the ordering of eigenvalues according to (3.4) ensures that the POD modes are ranked in terms of their energy content. The relative contribution of the *i*th POD mode to the total energy content of the flow is given by

$$\text{relative energy of } i^{\text{th}} \text{ mode} = \frac{\lambda^{(i)}}{\sum_k \lambda^{(k)}}. \tag{3.5}$$

The onset of instability is identified when the number of dominant POD modes that capture 99 % of the total energy of the signal deviates significantly from the number of modes
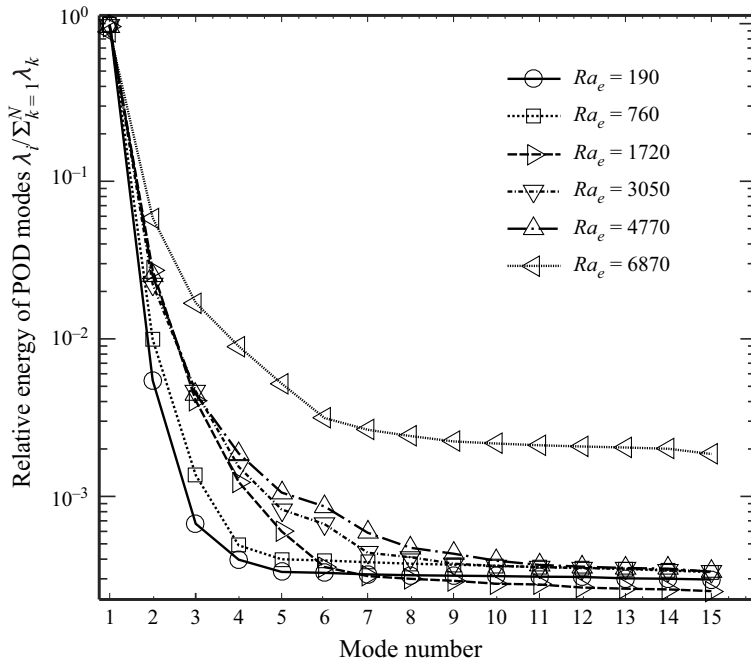
Figure 4. The relative energy contribution of the first 15 POD modes at varying values of electric Rayleigh number (Ra_e). At low values of $Ra_e = 190$ and 760, the first POD mode contributes approximately 99 % of the total energy of the signal. For $Ra_e = 1720$, the energy distribution shows significant deviation from that at lower Ra_e values, indicating the presence of instability. At even higher Ra_e, a higher number of POD modes are dominant, corresponding to a stronger instability.

corresponding to the stable flow. The dominant flow structures also help in differentiating the unstable and stable flows. We performed POD analysis using $N = 25$ time-resolved snapshots of the fluorescent scalar field captured in every experiment. The data were analysed in a reference frame moving with the mean EOF velocity. To this end, we shifted the pixels in every snapshot by estimating the mean EOF velocity from the advection of the passive scalar. This resulted in a new set of snapshots wherein the conductivity gradient appears stationary and POD was performed on this set of images. Figure 4 shows the relative contribution of the first fifteen POD modes to the total energy content of the signal for $Ra_e = 190$–6870. The singular values corresponding to dominant POD modes that cumulatively contribute to 99 % of the overall energy content of the signal are presented in table 2. For all values of Ra_e, the first POD mode is the most dominant mode with more than 90 % contribution to the total energy content of the signal. At $Ra_e = 190$, the time-resolved snapshots have POD modes with only one dominant mode, as the flow is stable. Even at $Ra_e = 760$, the energy contribution of the second POD mode is less than 1 %. At $Ra_e = 1720$, a second mode with significant contribution appears in the flow, as shown in figure 4, suggesting the presence of instability. As Ra_e is further increased, more dominant modes appear in the flow. At $Ra_e = 3050$ and 4770, there are three dominant modes that altogether sum up to 99 % of the total energy, whereas, at $Ra_e = 6870$, there are six most energetic modes.

We analysed the spatial POD modes for all Ra_e to identify whether the dominant POD modes correspond to coherent structures and not random experimental noise. In figure 5, we present the first seven spatial POD modes for $Ra_e = 760$, 1720, 3050 and 6870. The first

Ra_e	Relative energy of each POD mode				
	1	2	3	4	5
190	0.99	—	—	—	—
760	0.9827	0.0099	—	—	—
1720	0.9630	0.0272	—	—	—
3050	0.9653	0.0222	0.0045	—	—
4770	0.9615	0.0251	0.0047	—	—
6870	0.8877	0.0585	0.0169	0.009	0.005

Table 2. Relative energy of obtained POD modes for varying values of electric Rayleigh number.
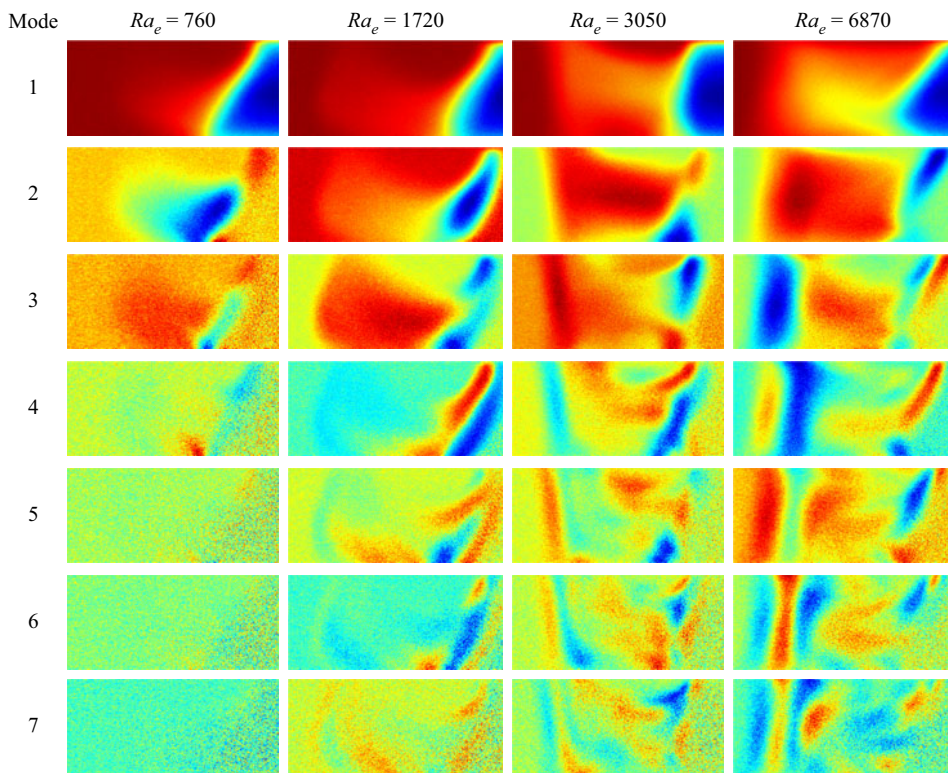

Figure 5. POD modes showing the coherent structures observed in experiments at different electric Rayleigh numbers (Ra_e). The flow is stable at low $Ra_e = 760$, and only the first two modes are dominant. At $Ra_e = 1720$ and 3050, the flow is unstable, and the coherent structures appear throughout the low-conductivity zone. At very high value of $Ra_e = 6870$, the instability is stronger and is characterised by more energetic coherent structures.

POD mode for all Ra_e values is equivalent to the ensemble mean of the experimental snapshots, while the higher modes correspond to the fluctuations in the flow. At a low value of $Ra_e = 760$, the second mode, which contributes less than 1 % to the total energy, shows localised fluctuations near the conductivity gradient. Comparing the POD modes with time-resolved snapshots in figure 3, it is evident that the second mode at $Ra_e = 760$ corresponds to slight diffusion of the conductivity gradient in an otherwise stable flow. The third and higher POD modes at $Ra_e = 760$ have significant experimental noise and they do not show meaningful coherent structures.

925 A14-12

At higher values of $Ra_e = 1720$, 3050 and 6870, besides the dominant first mode, a large number of modes (modes 2 to 7) corresponding to different length scales of fluctuations are present. These modes show perturbations in the scalar concentration field throughout the low-conductivity zone, indicating the presence of an instability. In particular, mode 3 for $Ra_e = 1720$ and mode 2 for $Ra_e = 3050$ and 6870 clearly show the high-conductivity stream that is drawn into the low-conductivity electrolyte zone by non-uniform EOF. The higher modes are characterised by finer spatial structures with spanwise variations in the scalar concentration field. These modes correspond to the spanwise oscillations of the high-conductivity stream within the low-conductivity zone.

4. Numerical simulation

The experiments reported in § 3 provide conclusive evidence of EKI in a microchannel flow with streamwise conductivity gradients under an externally applied electric field. The instability occurs over a time scale of order 10 ms and measurements other than visualisation of a passive scalar in such a microfluidic system is rather challenging. Therefore, to gain a mechanistic understanding of the EKI phenomena, we performed numerical simulations of an electrokinetic system similar to that in the experiments. We begin this section by providing a brief description of the mathematical model and the numerical method used to simulate the instability. Subsequently, we present the simulation predictions at varying values of electric Rayleigh number (Ra_e).

4.1. *Mathematical model*

The flow velocity u in an incompressible fluid flow driven by an electric field obeys the continuity equation,

$$\nabla \cdot u = 0. \tag{4.1}$$

The conservation of momentum is described by the Navier–Stokes equations with an additional electric body force term

$$\rho \frac{\partial u}{\partial t} + \rho u \cdot \nabla u = -\nabla p + \eta \nabla^2 u + \rho_f E. \tag{4.2}$$

Here ρ, p and η denote the density, pressure and dynamic viscosity of the liquid, respectively. In this equation, $\rho_f E$ is the electric body force which results from the coupling of the free charge density ρ_f with the local electric field E in the fluid (Melcher & Schwarz 1968). We have retained the inertia terms in the momentum equation because the electroviscous velocity, defined by (2.6a,b), in our experiments corresponds to Reynolds number $Re = \rho U_{ev} w / \eta$ of $O(1)$. In particular, for a typical electric field of $E = 30$ kV m^{-1}, the electroviscous velocity from (2.6a,b) is $U_{ev} = 31$ mm s^{-1}, and $Re = 1.6$. Assuming that the electrolyte is a linear dielectric with spatially uniform dielectric permittivity ϵ, the free charge density is given by Gauss' law,

$$\rho_f = \epsilon \nabla \cdot E. \tag{4.3}$$

The electric body force in (4.2) can therefore be expressed in terms of the local electric field as $\rho_f E = \epsilon (\nabla \cdot E) E$.

The local electric field E required to obtain the electric body force on the fluid depends on the spatial distribution of ions in the electrolyte. The transport of cations ($+$) and

anions $(-)$ in a binary electrolyte is governed by the electromigration–advection–diffusion equations,

$$\frac{\partial c_{\pm}}{\partial t} + \nabla \cdot (\boldsymbol{u} c_{\pm} + \mu_{+} c_{\pm} \boldsymbol{E} - D_{\pm} \nabla c_{\pm}) = 0. \tag{4.4}$$

Here, c denotes the ion concentration, D the molecular diffusivity and μ the electrophoretic mobility. The diffusivity of ions is related to their electrophoretic mobility by Einstein's relation $D_{\pm} = \mu_{\pm} kT/(z_{\pm}e)$, where k is the Boltzmann constant, T the absolute temperature and e the elementary charge. The above set of transport equations can be simplified by assuming that the electrolyte solution is approximately electroneutral, $z_{+}c_{+} \simeq -z_{-}c_{-}$ (Levich 1962; Chen *et al.* 2005). Multiplying the transport equations (4.4) for cations and anions with $z_{\pm}F$ (F is the Faraday constant) and summing them up, while invoking the electroneutrality assumption, yields

$$\nabla \cdot (\sigma \boldsymbol{E} - \nabla S) = 0, \quad S = z_{+} D_{+} c_{+} F + z_{-} D_{-} c_{-} F, \tag{4.5}$$

where $\sigma = (z_{+}\mu_{+}c_{+} + z_{-}\mu_{-}c_{-})F$ is the electrical conductivity of the electrolyte. Equation (4.5) describes the conservation of total current which is the sum of ohmic current $\sigma \boldsymbol{E}$ and the diffusion current $-\nabla S$. As shown by Chen *et al.* (2005), typically for a strong electric field of $O(10 \text{ kV m}^{-1})$ such as that in our experiments, the ohmic current is significantly larger than the diffusion current. Therefore, the diffusion current can be neglected and (4.5) simplifies to Ohm's law,

$$\nabla \cdot (\sigma \boldsymbol{E}) = 0. \tag{4.6}$$

The governing equation for conductivity σ is derived by multiplying the transport equations (4.4) for cations and anions with $z_{\pm}\mu_{\pm}F$ and by adding the two equations. Eliminating the electric field $\boldsymbol{E}$ from the resulting equation using (4.5) and using the electroneutrality assumption leads to a convection–diffusion equation for the conductivity field,

$$\frac{\partial \sigma}{\partial t} + \boldsymbol{u} \cdot \nabla \sigma = D_{eff} \nabla^{2} \sigma, \quad D_{eff} = \frac{(z_{+} - z_{-})D_{+}D_{-}}{z_{+}D_{+} - z_{-}D_{-}}. \tag{4.7}$$

For a binary electrolyte having ions with valences $z_{+} = -z_{-}$, the effective diffusivity is given by $D_{eff} = 2D_{+}D_{-}/(D_{+} + D_{-})$. Lastly, due to the low current density and displacement current in electrokinetic flows, the electric field can be assumed to be quasistatic and hence irrotational,

$$\nabla \times \boldsymbol{E} = 0. \tag{4.8}$$

Therefore, the electric field is related to the electric potential ϕ by $\boldsymbol{E} = -\nabla \phi$.

Equations (4.1)–(4.3), (4.6)–(4.8) describe the electric field-driven flow in an electrolyte with conductivity gradients. Note that in the derivation of these governing equations, we have used the electroneutrality assumption for mass conservation of ions but included an electric body force due to free charge in the momentum equation (4.2). This is due to the fact that the conductivity variation leads to gradients in the local electric field which in turn lead to accumulation of free charge in the fluid. The difference in the concentration of cations and anions associated with this accumulated free charge is small compared with the bulk ion concentrations, therefore it can be ignored for mass conservation. However, the coupling of a small amount of charge with a strong electric field results in an appreciable electric body force that cannot be neglected (Hoburg & Melcher 1977; Ramos 2011). Therefore, for a given conductivity field, we use Ohm's law (4.6) to solve for the electric
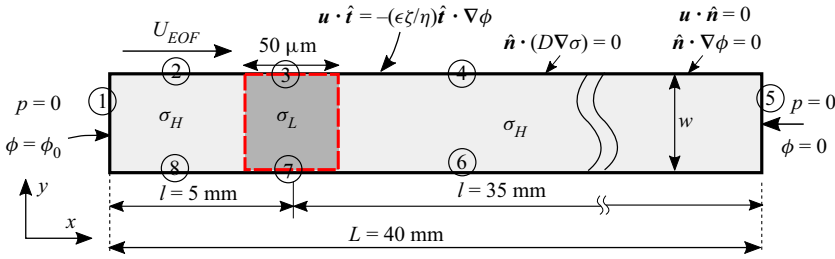
Figure 6. Sketch of the two-dimensional computational domain showing various geometric parameters and boundary conditions. A low-conductivity zone with a length equal to the channel width is initially surrounded by two high-conductivity electrolyte zones. The length and the width of the computational domain are the same as those of the microchip used in the experiments. The encircled numbers refer to the boundaries of the model geometry. The boundary conditions corresponding to these numbers are described in detail in table 3.

field, which is then used to determine the free charge density ρ_f from Gauss' law (4.3). The free charge density is therefore given by

$$\rho_f = \epsilon \nabla \cdot E = -\epsilon E \cdot \nabla \sigma / \sigma. \tag{4.9}$$

This equation clearly shows that free charges are induced in the regions with conductivity gradients (Wang, Yang & Zhao 2016).

We solved the governing equations in a two-dimensional computational domain, shown schematically in figure 6. We choose the following reference scales to non-dimensionalise the governing equations:

$$\left.\begin{array}{c} [x, y] = w, \quad [\phi] = \phi_0, \quad [E] = E_0 = \dfrac{\phi_0}{L}, \quad [u] = U_{ev} = \dfrac{\epsilon E_0^2 w}{\eta}, \\[2mm] [t] = \dfrac{w}{U_{ev}}, \quad [p] = \epsilon E_0^2, \quad [\sigma] = \sigma_L. \end{array}\right\} \tag{4.10}$$

Here, ϕ_0 is the voltage difference applied across the channel and L is the channel length, as shown in figure 6. This scaling yields the following set of non-dimensionalised governing equations:

$$\nabla \cdot u = 0, \tag{4.11}$$

$$\frac{Ra_e}{Sc} \frac{Du}{Dt} = -\nabla p + \nabla^2 u + \nabla^2 \phi \nabla \phi, \tag{4.12}$$

$$\nabla \cdot (\sigma \nabla \phi) = 0, \tag{4.13}$$

$$\frac{D\sigma}{Dt} = \frac{1}{Ra_e} \nabla^2 \sigma. \tag{4.14}$$

Here, Ra_e is the electric Rayleigh number, and Sc is the Schmidt number defined as

$$Ra_e = \frac{\epsilon E_0^2 w^2}{\eta D_{eff}} \quad \text{and} \quad Sc = \frac{\eta}{\rho D_{eff}}. \tag{4.15a,b}$$

4.2. *Initial and boundary conditions and numerical method*

The initial and boundary conditions used to simulate the EKI are depicted in the schematic of the computational domain in figure 6. Initially, a plug of low-conductivity electrolyte

Variable	Boundary	Expression
p	1, 5	$p = 0$
$\boldsymbol{u}$	2, 3, 4, 6, 7, 8	$\boldsymbol{u} \cdot \hat{\boldsymbol{t}} = -(\epsilon\zeta/\eta)\hat{\boldsymbol{t}} \cdot \nabla\phi$
		$\boldsymbol{u} \cdot \hat{\boldsymbol{n}} = 0$
ϕ	1	$\phi = \phi_0$
	5	$\phi = 0$
	2, 3, 4, 6, 7, 8	$\hat{\boldsymbol{n}} \cdot \nabla\phi = 0$
σ	1, 5	$\sigma = \sigma_H$
	2, 3, 4, 6, 7, 8	$\hat{\boldsymbol{n}} \cdot (D\nabla\sigma) = 0$

Table 3. Boundary conditions corresponding to the computational domain shown in figure 6.

is surrounded by two zones of high-conductivity electrolyte. In the beginning, the flow configuration remains stationary as no potential difference is applied across the channel. At $t = 0$, a potential difference ϕ_0 is applied which drives fluid flow in the microchannel. The physical dimensions of the channel and the low-conductivity plug in the simulations were the same as those in the experiments. In this work, the experiments were designed to ensure negligible flow in the N and S channels of the microfluidic device (figure 2). Therefore, N and S channels were not included in the computational domain.

The boundary conditions used in the simulations are summarised in table 3. The inlet and the exit of the channel are maintained at the same pressure $p = 0$. The tangential electroosmotic slip boundary condition (2.4) is imposed on the impermeable channel walls to model the EOF. No flux boundary conditions for conductivity and electric field are applied on the channel walls. The conductivity at the channel ends is kept fixed at σ_H. The conductivity of the electrolyte solutions in the simulations is the same as those of electrolytes used in the experiments. The values of various physical parameters used for the simulations are provided in table 1. The value of zeta-potential ($\zeta = -74.7$ mV) used in the electroosmotic slip boundary condition (2.4) was estimated using the current monitoring method (Babar, Dubey & Bahga 2020) . For this value of zeta-potential and transverse channel dimensions of order 10 µm, the Bikerman number, defined as $Bi = \delta\,\mathrm{e}^{|ze\zeta/kT|/2}$, is negligible ($Bi \ll 1$), where δ is the ratio of electric double layer (EDL) thickness to the characteristic width of the microchannel (Schnitzer & Yariv 2012). In this $Bi \ll 1$ limit, surface conduction through the EDL (Bikerman 1940; O'Brien & Hunter 1981) can be neglected. Therefore, the only effect of the EDL is to provide an electroosmotic slip velocity at the channel walls. Note that we have chosen the channel dimensions and the boundary conditions to be the same as those in the experiments to validate our simulations. In this respect, our simulations are more realistic than the EKI simulations in a periodic domain presented by Santos & Storey (2008). The periodic boundary conditions cannot be realised in experiments, and hence the simulations of Santos & Storey (2008) cannot be directly verified with experimental observations.

The governing equations described in § 4.1, along with the above mentioned initial and boundary conditions, were solved numerically using a commercial simulation package, COMSOL Multiphysics (COMSOL AB, Stockholm, Sweden), which is based on the finite element method. We implemented the governing equations and the associated initial and boundary conditions using the solver's in-built laminar flow and partial differential equation (PDE) modules. We used the laminar flow module to incorporate the continuity and momentum equations and used the PDE module to incorporate the governing

925 A14-16

equations for electric field and electrolyte conductivity. The choice of COMSOL package was based on its capability to accurately simulate chaotic electrokinetic flows involving a wide range of spatio-temporal scales (Karatay, Druzgalski & Mani 2015). An unstructured grid of triangular elements is used to discretise the computational domain. To reduce the computational time, we use a coarse grid everywhere except in a small region surrounding the low-conductivity zone,where a fine mesh has been employed. The coarse mesh has a uniform element size of 10 μm, whereas the fine mesh has a minimum and maximum element size of 0.4 μm and 1 μm, respectively. A time-dependent multifrontal massively parallel sparse direct solver is employed for transient calculations. The time stepping is performed using a second-order implicit backward difference scheme.

5. Simulation results

We performed simulations at various electric fields (ϕ_0/L) in the range 10–30 kV m^{-1} while keeping the conductivity ratio fixed at $\gamma = 10$. In terms of dimensionless numbers, the electric Rayleigh number Ra_e is varied by varying the electric field, while Sc and γ are kept fixed. For consistency, we have used the same definition of Ra_e for presenting the simulation and experiment results. In contrast to the experiments, the simulations are two-dimensional wherein viscous stresses due to velocity gradients in the depth direction are absent. Therefore, we expect the simulations to predict instability at lower values of Ra_e compared with that in the experiments.

We begin by presenting the qualitative features of instability predicted by the simulations at various electric field values (or electric Rayleigh numbers Ra_e). Figure 7 shows the time evolution of scalar conductivity field predicted by the simulations at three different electric fields of 10, 20 and 25 kV m^{-1}, corresponding to $Ra_e = 190$, 760 and 1190. Initially, the low-conductivity zone is surrounded by two regions of high-conductivity electrolyte. Thus, two sharp interfaces exist initially between the high- and low-conductivity regions. At $t = 0$, an external electric field pointing from the W to E ends of the channel is applied. At low $Ra_e = 190$, the simulation predicts that the flow is stable, but the non-uniform EOF associated with the heterogeneous electrolyte conductivity deforms the conductivity gradients. As shown in figure 7(*a*), the non-uniform EOF draws the high-conductivity electrolyte present on the right into the low-conductivity zone. Consequently, the initially straight interface between the high- and low-conductivity zones on the right deforms into a triangular shape. However, due to a relatively low electric field, the conductivity field remains symmetric across the channel centreline and diffuses over time without exhibiting any instability.

Figure 7(*b*) shows the spatio-temporal evolution of the conductivity field at a higher electric field of 20 kV m^{-1} corresponding to $Ra_e = 760$. In this case, the leading interface separating the high- and the low-conductivity zones deforms faster due to non-uniform EOF. At $t = 5$ ms, a thin stream of high-conductivity electrolyte is drawn into the low-conductivity zone. This results in a configuration wherein the conductivity gradients within the low-conductivity plug become orthogonal to the electric field. At a later time, an instability is observed within the low-conductivity zone, which resembles the EKI in microchannel flow with an orthogonal conductivity gradient and electric field (Posner & Santiago 2006; Dubey *et al.* 2017). The instability is characterised by asymmetric oscillations of the thin stream of high-conductivity electrolyte within the low-conductivity plug, as was also observed in the experiments. At an even higher electric field of 25 kV m^{-1} ($Ra_e = 1190$), figure 7(*c*) shows that the unstable motion appears more chaotic. In particular, once the instability sets in, the high-conductivity electrolyte is drawn into the low-conductivity zone at various locations on the leading interface. The chaotic flow leads
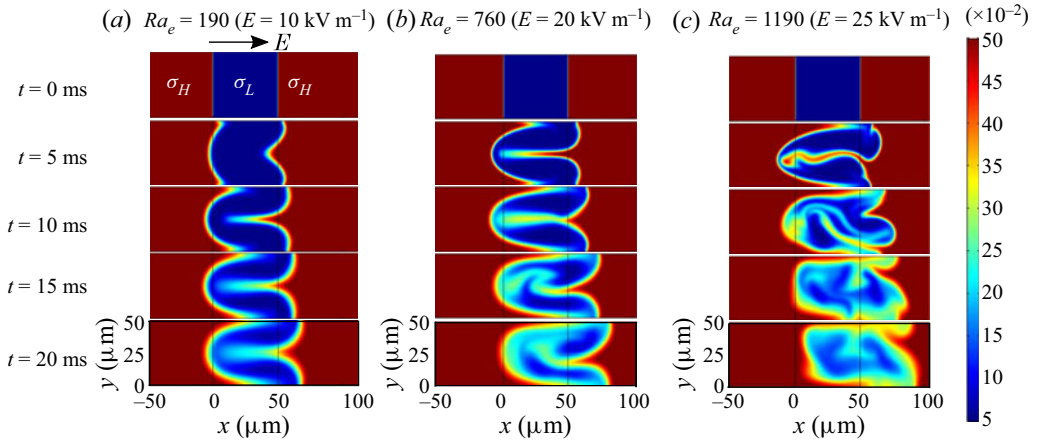
Figure 7. Representative snapshots showing simulated evolution of conductivity field with time for varying electric Rayleigh numbers Ra_e. The high-conductivity regions are shown in red colour and the low-conductivity regions are shown in blue colour. (*a*) At low $Ra_e = 190$, the flow remains stable, and a thin stream of high-conductivity electrolyte is drawn into the low-conductivity zone due to non-uniform EOF. (*b*) At an increased value of $Ra_e = 760$, an instability sets in and the stream of high-conductivity electrolyte within the low-conductivity electrolyte shows asymmetric fluctuations. (*c*) The instability becomes more chaotic at $Ra_e = 1190$, and it fades out over time due to the rapid dispersion of conductivity gradients. The instability is confined to the low-conductivity zone and lasts for a short time duration of order 20 ms.

to rapid mixing within the low-conductivity zone. Note that the instability is confined to the low-conductivity zone, where strong local electric field and conductivity gradients lead to a destabilising electric body force on the fluid. The instability features predicted by the simulation are qualitatively similar to those observed in the experiments, described earlier in § 3. Simulations and experiments show that the instability sets in within a few milliseconds and lasts for a time duration of order 20 ms. This can be attributed to the fact that the time scale corresponding to the destabilising electroviscous flow is $\tau_{ev} = 1.6$ ms for an electric field of 30 kV m^{-1}. The flow instability causes rapid mixing of high- and low-conductivity zones within a short time duration, and the instability fades away when the conductivity gradients diminish. Thereafter, the dispersed low-conductivity plug slowly advects along the main channel due to EOF over a time scale of $\tau_{eof} = 32$ ms and simultaneously diffuses into the adjoining high-conductivity zones over a time scale of $\tau_{diff} = 2.75$ s.

5.1. *The role of electric body force and physical mechanism of instability*

Having discussed the qualitative features of the instability through the evolution of the conductivity field, we now discuss the role of the electric body force in destabilising the microchannel flow and the physical mechanism of instability. In figures 8 and 9 we present the simulated time evolution of the conductivity field, free charge, electric field and the streamlines of flow for $Ra_e = 190$ and 1190, respectively. At the low electric field corresponding to $Ra_e = 190$, the conductivity and the flow fields remain symmetric about the centreline of the channel for all times, as shown in figure 8. The non-uniform electroosmotic slip velocity at the channel walls due to streamwise conductivity gradients results in two large symmetric vortices in the low-conductivity region. This recirculating fluid motion draws the high-conductivity electrolyte into the low-conductivity region.
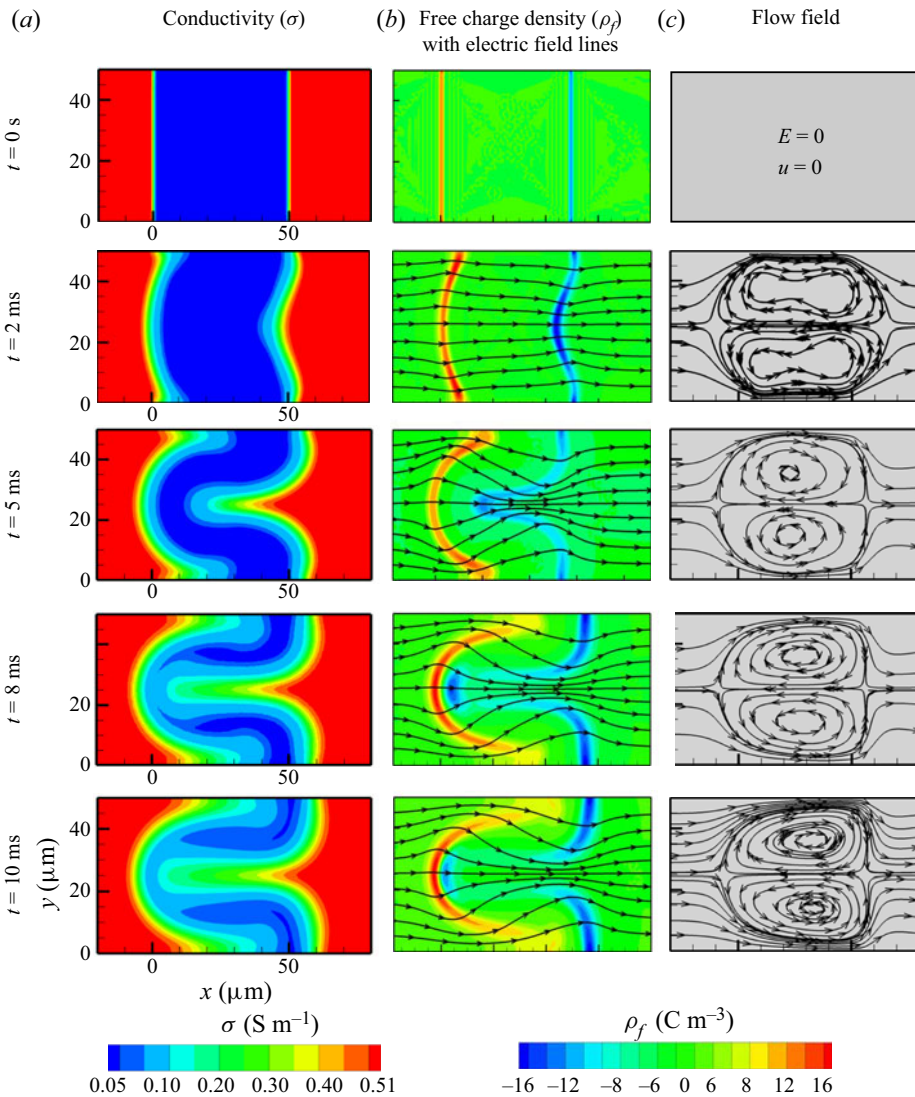
925 A14-18

Figure 8. Simulated evolution of the conductivity field, free charge density, electric field and streamlines for electric Rayleigh number $Ra_e = 190$. For better visualisation, a small part (150 μm × 50 μm) of the computational domain is shown here. (*a*) The temporal evolution of the conductivity field shows that the flow remains stable at low electric field. The flow recirculation draws in the high-conductivity electrolyte into the low-conductivity zone. (*b*) The free charge is induced in the regions with conductivity gradients and this charge couples with the local electric field to apply a body force on the fluid. At $Ra_e = 190$, the body force is not strong enough to destabilise the flow. (*c*) Consequently, the flow remains symmetric about the centreline as depicted by the streamlines.

As shown in figure 8(*b*), a negative (positive) free charge is induced in the regions with conductivity gradients, where the electric field points from low (high) to high (low) conductivity regions. The electric body force on the fluid acts only in the regions with free charge. At $Ra_e = 190$, the electric body force is not strong enough to produce sufficiently high electroviscous velocity to destabilise the flow. Therefore, the flow remains symmetric about the centreline, and the conductivity gradients diffuse over time.
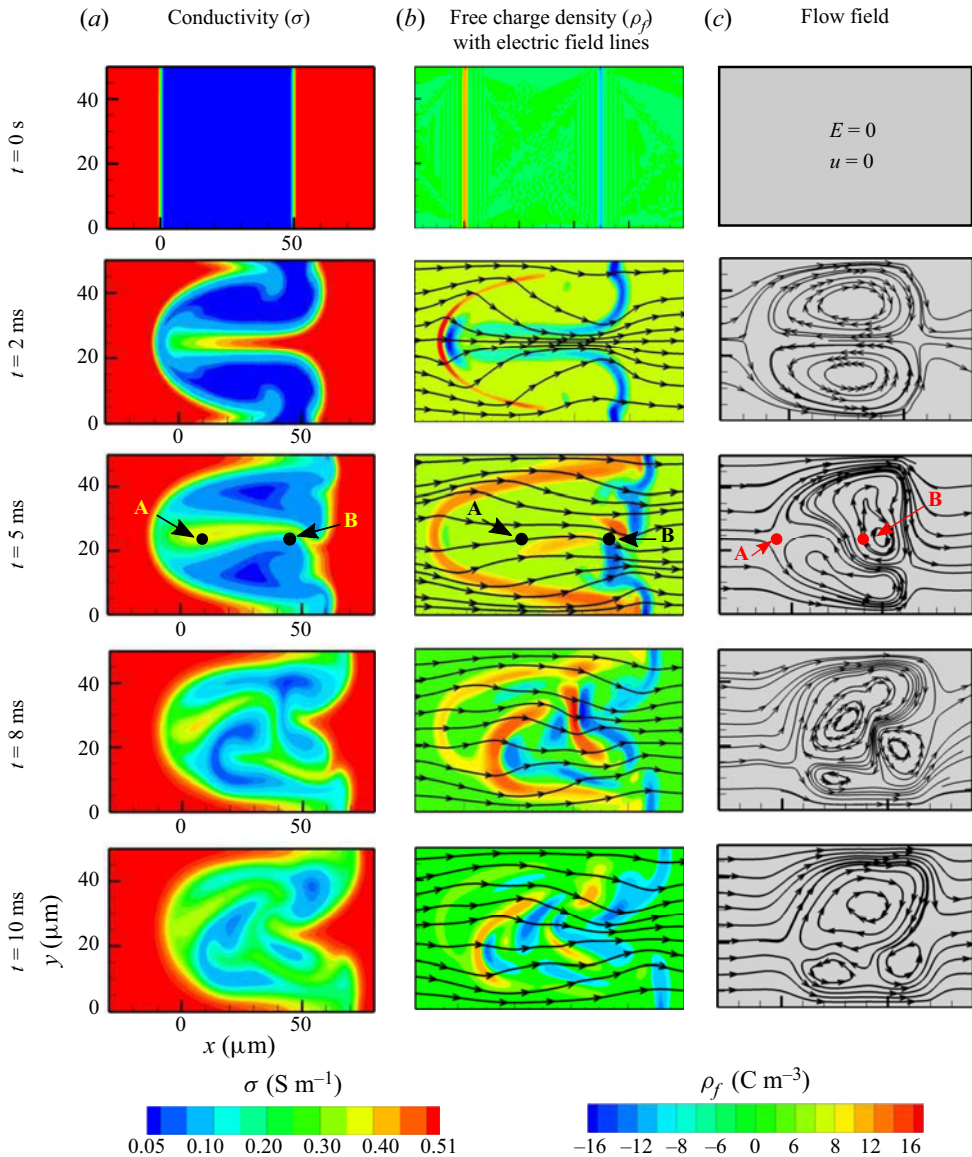
Figure 9. Simulated conductivity field, free charge density, electric field and flow field for $Ra_e = 1190$. (a) Instability at high Ra_e leads to rapid mixing of high- and low-conductivity solutions. The instability is characterised by an asymmetry in charge distribution and electric field as shown in (b) and asymmetric vortices as shown by the streamlines in (c). During the initial phase of the instability ($t = 2$ ms), the high-conductivity solution is drawn into the low-conductivity zone. The high-conductivity stream within the low-conductivity zone gets disturbed ($t = 5$ ms) and leads to a redistribution of charge and local electric field. The resulting electric body force drives a flow which further amplifies the disturbances.

At the high electric field corresponding to $Ra_e = 1190$, the flow recirculation is stronger, and it quickly draws the high-conductivity electrolyte into the low-conductivity plug, as shown in figure 9. Consequently, within the low-conductivity plug, a new configuration is created wherein a high-conductivity stream flows between two adjoining streams of low-conductivity and the conductivity gradient is orthogonal to the electric field. This flow

configuration resembles that in electrokinetic mixers wherein a high-conductivity stream flowing between two low-conductivity sheath streams destabilises upon applying a high axial electric field (Posner & Santiago 2006; Dubey *et al.* 2017). EKI in this flow configuration has been widely studied through experiments (Posner & Santiago 2006; Dubey *et al.* 2017) and simulations (Li, Delorme & Frankel 2016). Therefore, after the high-conductivity electrolyte is drawn into the low-conductivity plug by the recirculatory flow, the flow destabilises due to the same physical mechanism as in electrokinetic mixing experiments of Posner & Santiago (2006). The symmetric vortices at early times ($t = 2$ ms) give way to asymmetric vortices associated with the instability ($t = 5$ ms and later). The instability further deforms the conductivity gradients and establishes an intricate flow pattern characterised by more than two eddies.

The destabilising nature of the electric body force can be understood from the simulation predictions at $t = 2$ and 5 ms in figure 9. At $t = 2$ ms, a high-conductivity stream is drawn into the low-conductivity plug. From (4.9) it is evident that a negative (positive) charge is induced in the region where the local electric field has a component that points from the low (high) conductivity region to the high (low) conductivity region. Consequently, as shown in figure 9(*b*) at $t = 2$ ms, a negative charge is induced on the interface of the high-conductivity stream within the low-conductivity plug. Any disturbance of this high-conductivity stream leads to a change in the charge distribution at the interface of the stream, as observed at $t = 5$ ms in figure 9. The free charge at the interface of the high-conductivity stream couples with the local electric field and drives an electroviscous flow which further amplifies the disturbance in the conductivity field, as shown by the streamlines. For example, the high-conductivity stream is perturbed downwards at point A and upwards at point B at $t = 5$ ms in figure 9. This disturbance causes a body force that drives a downward flow at A and upward flow at B, further amplifying the disturbance. Consequently, the instability is characterised by a wavy structure of the high-conductivity stream within the low-conductivity plug. Similar wavy structures have been observed in EKI in a different microchannel flow configuration with orthogonal conductivity gradient and electric field (Dubey *et al.* 2017). At such high Ra_e, the electroviscous flow is strong enough to amplify the disturbances in the conductivity field faster than the rate at which conductivity gradients diffuse, resulting in the instability. The instability is localised in the low-conductivity plug because the local electric field is an order of magnitude greater as compared with that in the high-conductivity region attributed to the conductivity ratio $\gamma = \sigma_H/\sigma_L$.

To further highlight the role of electric body force in destabilising the flow, we performed an additional numerical simulation by ignoring the electric body force term in the momentum equation (4.2). In figure 10, we compare the time evolution of the maximum transverse velocity (v_{max}) at the channel centreline at $Ra_e = 1720$ predicted by the simulations with and without the electric body force term. The instability is characterised by asymmetric flow about the channel centreline, which is otherwise symmetric in the stable regime. Therefore, v_{max} can be considered as a measure of instability. As shown in figure 10, v_{max} remains low when the electric body force term is ignored and the flow remains stable. However, for the same value of Ra_e inclusion of the electric body force in the momentum equation results in an unstable flow, with four orders of magnitude higher maximum transverse velocity v_{max} at the centreline. The instantaneous snapshots at $t=10$ ms shown in the inset of figure 10 clearly indicate a stable flow in the absence of electric body force. We note that these simulations show that the orthogonal configuration develops irrespective of whether electric body force is included in the momentum equation or not. Moreover, when electric body force is included in the
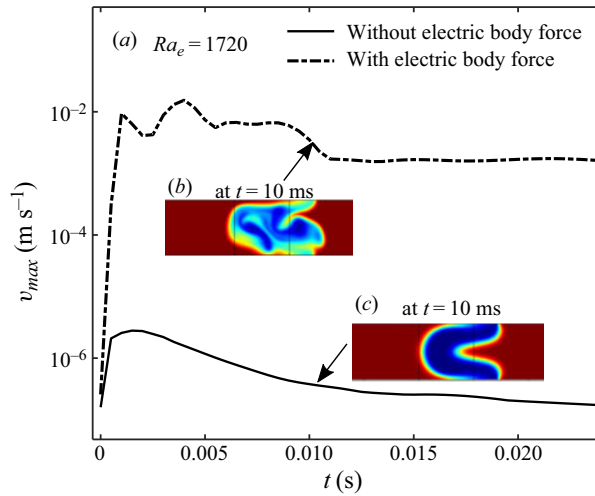
Figure 10. Comparison of simulations performed with and without incorporating the electric body force term in the momentum equation at $Ra_e = 1720$. (*a*) The temporal evolution of the maximum transverse velocity v_{max} at the channel centreline shows that v_{max} remains low when electric body force is ignored, and the flow remains stable as shown in (*c*). (*a,b*) However, upon incorporating the electric body force, at the same value of Ra_e, the simulation predicts an instability with four orders of magnitude higher v_{max}.

simulations, the flow destabilises only after the non-uniform EOF creates a configuration wherein the electric field and conductivity gradient are orthogonal. This suggests that the generation of orthogonal configuration is solely due to non-uniform EOF, whereas instability results from the destabilising electroviscous flow.

5.2. *Critical Ra_e: comparison between simulations and experiments*

So far, we have seen that the electric field-driven microchannel flow in the presence of streamwise conductivity gradients becomes unstable at high electric fields. Unlike various other studies of electrokinetic and electrohydrodynamic instabilities (Hoburg & Melcher 1976; Baygents & Baldessari 1998; Lin *et al.* 2004; Chen *et al.* 2005; Sharan *et al.* 2017) where the base-state flow was stationary, such a steady base state does not exist in the current case. Rather, the conductivity field is governed by the transient advection due to non-uniform EOF and diffusion. In the absence of a steady base state, the critical electric Rayleigh number for the onset of instability cannot be determined through a linear stability analysis. Therefore, we consider the maximum transverse velocity (v_{max}) at the channel centreline, (predicted by the simulation), to determine the onset of instability. The stable flow regime is characterised by negligible v_{max} as the flow is symmetric across the centreline. On the other hand, asymmetry associated with unstable flow field leads to finite values of v_{max}. Figure 11(*a*) shows the variation of v_{max} with time for varying electric Rayleigh numbers obtained from simulations. At the low value of electric field corresponding to $Ra_e = 190$, v_{max} remains relatively negligible over time, suggesting a stable flow. At $Ra_e = 430$ and above, v_{max} grows exponentially to a peak value within a short time duration and thereafter varies slowly as the instability fades away due to dispersion of conductivity gradients. The peak value of v_{max} and the growth rate of the instability increases with an increase in Ra_e. Besides an exponential increase in v_{max} at high Ra_e, figure 11(*a*) also shows fluctuations in v_{max} due to the instability.
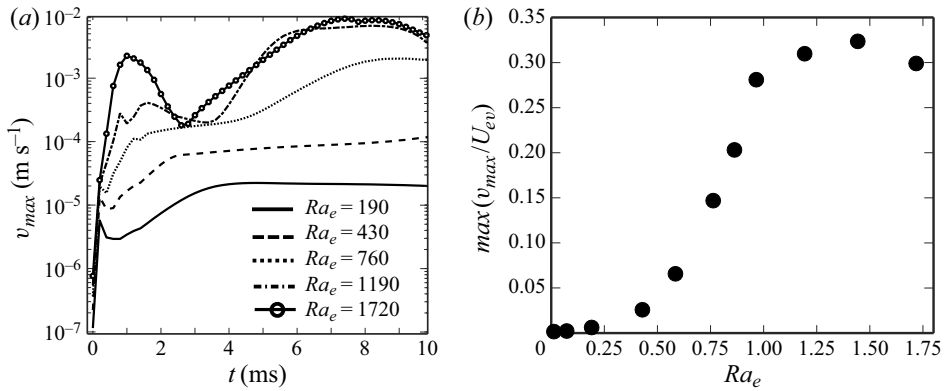
925 A14-22

Figure 11. Simulated variation of the maximum transverse velocity (v_{max}) at the channel centreline with time for varying values of Ra_e. (*a*) Variation of v_{max} vs t. The low values of v_{max} for $Ra_e = 190$ correspond to a stable flow regime. For $Ra_e = 430$ and above, v_{max} initially grows exponentially and attains an appreciable magnitude, indicating the presence of instability. (*b*) The variation of the maximum, dimensionless transverse velocity at the centreline v_{max}/U_{ev} predicted over time with Ra_e, suggests that the critical Ra_e for the onset of instability lies in the range of 190–430.

In figure 11(*b*), we present the variation of the maximum predicted value of v_{max}/U_{ev} over the simulation times for different Ra_e. The maximum dimensionless transverse velocity v_{max}/U_{ev} is negligible for $Ra_e = 190$ and below, and becomes significant for $Ra_e = 430$ and above. Therefore, the critical value of Ra_e lies between 190 and 430. Compared with the two-dimensional simulations, the instability in experiments sets in at a higher value around $Ra_e = 1720$. Unlike in two-dimensional simulations, the viscous stresses due to velocity gradients in the depth direction can be expected to be dominating in the experiments. Consequently, the flow destabilises at higher electric field values and Ra_e in the experiments.

For a better comparison of the critical Ra_e in experiments and simulations, we define Ra_e in experiments using the channel depth instead of the width as the characteristic length scale. The modified electric Rayleigh number based on the channel depth is given by $Ra_{e,d} = \epsilon E^2 d^2/(\eta D_{eff})$. Because $Ra_{e,d}/Ra_e = (d/w)^2$ and in experiments $d/w = 0.4$, the critical value of $Ra_{e,d}$ in experiments is 275 (corresponding to $Ra_e = 1720$). This value of critical $Ra_{e,d}$ is in quantitative agreement with critical value of Ra_e predicted by the two-dimensional simulations. The simulations also show similar instability features as observed in the experiments. Therefore, the instability observed in our experiments occurs due to the same physical mechanism as that in the simulations. We also note that the critical electric Rayleigh number obtained in our work is of the same order of magnitude as obtained by Posner & Santiago (2006) ($Ra_e = 205$) in a configuration wherein the electric field was applied orthogonal to the conductivity gradient. This is attributed to the fact that despite the differences in the base state, the EKI in the presence of streamwise conductivity gradient develops by setting up a new configuration wherein electric field and conductivity gradient become orthogonal.

6. Conclusion

We have presented a detailed experimental and numerical study of the EKI that occurs when a strong electric field is applied across a streamwise conductivity gradient in a microchannel flow. We visualised the instability through high-speed imaging of a passive

scalar in a series of controlled experiments at varying electric fields. Subsequently, we analysed the time-resolved snapshots of the scalar concentration field using the POD technique to obtain a quantitative measure of the threshold electric field for the onset of instability, along with the corresponding coherent structures. The POD analysis of experimental data showed that the instability sets in at high electric field values corresponding to an electric Rayleigh number (Ra_e) of approximately 1720 for a conductivity ratio of $\gamma = 10$.

We have also performed high-resolution numerical simulations to elucidate the physical mechanism underlying the instability. The simulations show that the non-uniform EOF due to axially varying conductivity field causes a recirculating flow within the low-conductivityregion. This recirculatory fluid motion draws in the high-conductivity electrolyte into the low-conductivity region and creates a configuration where the local conductivity gradient is orthogonal to the applied electric field. These conductivity gradients in the presence of electric field result in free charge accumulation in the bulk solution, which in turn couples with the electric field to apply a destabilising body force on the fluid. The simulation predictions show that the instability is governed by the electroviscous effects that arise due to the interplay between the electric body force and the viscous force. The critical electric Rayleigh number for the onset of instability and the spatial features of instability predicted by the simulations are in good agreement with the experimental observations.

The flow configuration studied in the present work is usually employed to create axial gradients in the electric field during the sample stacking step in microchip electrophoresis. The sample-stacking step helps improve the detection sensitivity in electrophoresis by concentrating the analytes prior to separation. However, our experiments and simulations suggest that an EKI can arise during the sample-stacking step of microchip electrophoresis at electric field strengths typically used in practice. The onset of instability in sample stacking can lead to the rapid dispersion of analytes. Therefore, the instability can reduce the peak concentration of analytes and broaden the width of the analyte zones. Consequently, the instability can have a detrimental effect on the signal intensity and separation efficiency in electrophoresis, thereby negating the benefits of incorporating the sample-stacking step. While anecdotal evidence of such instability in microchip electrophoresis with sample stacking has been reported in the electrophoresis literature, we have provided conclusive empirical evidence of the existence of such instability. The present work strongly suggests that the effects of such instability should be considered while performing on-chip sample stacking. An investigation of the influence of EKI on the analyte dispersion during electrophoretic separation with sample stacking can be taken up as future work.

Declaration of interests. The authors report no conflict of interest.

Author ORCIDs.

Ⓓ Kaushlendra Dubey https://orcid.org/0000-0002-5574-1442;

Ⓓ Sanjeev Sanghi https://orcid.org/0000-0003-4400-5201;

Ⓓ Amit Gupta https://orcid.org/0000-0001-6709-7095;

Ⓓ Supreet Singh Bahga https://orcid.org/0000-0001-7277-9015.

REFERENCES

AJDARI, A. 1995 Electro-osmosis on inhomogeneously charged surfaces. *Phys. Rev. Lett.* **75** (4), 755–758.

ANDERSON, J.L. & IDOL, W. 1985 Electroosmosis through pores with nonuniformly charged walls. *Chem. Engng Commun.* **38** (3–6), 93–106.

BABAR, M., DUBEY, K. & BAHGA, S.S. 2020 Effect of surface conduction–induced electromigration on current monitoring method for electroosmotic flow measurement. *Electrophoresis* **41** (7-8), 570–577.

BAYGENTS, J.C. & BALDESSARI, F. 1998 Electrohydrodynamic instability in a thin fluid layer with an electrical conductivity gradient. *Phys. Fluids* **10** (1), 301–311.

BHARADWAJ, R. & SANTIAGO, J.G. 2005 Dynamics of field-amplified sample stacking. *J. Fluid Mech.* **543**, 57–92.

BIKERMAN, J.J. 1940 Electrokinetic equations and surface conductance. A survey of the diffuse double layer theory of colloidal solutions. *Trans. Faraday Soc.* **35**, 154–160.

CHEN, C.-H., LIN, H., LELE, S.K. & SANTIAGO, J.G. 2005 Convective and absolute electrokinetic instability with conductivity gradients. *J. Fluid Mech.* **524**, 263–303.

DANG, F., ZHANG, L., JABASINI, M., KAJI, N. & BABA, Y. 2003 Characterization of electrophoretic behavior of sugar isomers by microchip electrophoresis coupled with videomicroscopy. *Anal. Chem.* **75** (10), 2433–2439.

DEMEKHIN, E.A., NIKITIN, N.V. & SHELISTOV, V.S. 2013 Direct numerical simulation of electrokinetic instability and transition to chaotic motion. *Phys. Fluids* **25** (12), 122001.

DEMEKHIN, E.A., NIKITIN, N.V. & SHELISTOV, V.S. 2014 Three-dimensional coherent structures of electrokinetic instability. *Phys. Rev. E* **90** (1), 013031.

DUBEY, K., GUPTA, A. & BAHGA, S.S. 2017 Coherent structures in electrokinetic instability with orthogonal conductivity gradient and electric field. *Phys. Fluids* **29** (9), 092007.

DUBEY, K., GUPTA, A. & BAHGA, S.S. 2019 Scaling behavior in on-chip field-amplified sample stacking. *Electrophoresis* **40** (5), 730–739.

EL MOCTAR, A.O., AUBRY, N. & BATTON, J. 2003 Electro-hydrodynamic micro-fluidic mixer. *Lab on a Chip* **3** (4), 273–280.

FUKUNAGA, K. 1990 *Introduction to Statistical Pattern Recognition*, 2nd edn. Academic Press Professional, Inc.

GAUR, R. & BAHGA, S.S. 2017 Electrohydrodynamic instability of ion-concentration shock wave in electrophoresis. *Phys. Rev. E* **95** (6), 063109.

HERR, A.E., MOLHO, J.I., SANTIAGO, J.G., MUNGAL, M.G., KENNY, T.W. & GARGUILO, M.G. 2000 Electroosmotic capillary flow with nonuniform zeta potential. *Anal. Chem.* **72** (5), 1053–1057.

HOBURG, J.F. & MELCHER, J.R. 1976 Internal electrohydrodynamic instability and mixing of fluids with orthogonal field and conductivity gradients. *J. Fluid Mech.* **73** (2), 333–351.

HOBURG, J.F. & MELCHER, J.R. 1977 Electrohydrodynamic mixing an instability induced by collinear fields and conductivity gradients. *Phys. Fluids* **20**, 903–911.

HORVATH, A.L. 1985 *Handbook of Aqueous Electrolyte Solutions*. Halsted Press.

HUNTER, R.J. 1981 *Zeta Potential in Colloid Science: Principles and Applications*. Academic Press.

JACOBSON, S.C. & RAMSEY, J.M. 1995 Microchip electrophoresis with sample stacking. *Electrophoresis* **16** (1), 481–486.

KARATAY, E., DRUZGALSKI, C.L. & MANI, A. 2015 Simulation of chaotic electrokinetic transport: performance of commercial software versus custom-built direct numerical simulation codes. *J. Colloid Interface Sci.* **446**, 67–76.

KEELY, C.A., VAN DE GOOR, T.A.A.M. & MCMANIGILL, D. 1994 Modeling flow profiles and dispersion in capillary electrophoresis with nonuniform. zeta. Potential. *Anal. Chem.* **66** (23), 4236–4242.

LEVICH, V.G. 1962 *Physicochemical Hydrodynamics*. Prentice-Hall.

LI, Q., DELORME, Y. & FRANKEL, S.H. 2016 Parametric numerical study of electrokinetic instability in cross-shaped microchannels. *Microfluid Nanofluid* **20** (2), 29.

LIN, H. 2009 Electrokinetic instability in microchannel flows: a review. *Mech. Res. Commun.* **36**, 33–38.

LIN, H., STOREY, B.D., ODDY, M.H., CHEN, C.-H. & SANTIAGO, J.G. 2004 Instability of electrokinetic microchannel flows with conductivity gradients. *Phys. Fluids* **16**, 1922–1935.

LIN, H., STOREY, B.D. & SANTIAGO, J.G. 2008 A depth-averaged electrokinetic flow model for shallow microchannels. *J. Fluid Mech.* **608**, 43–70.

LUO, W.-J. 2009 Effect of ionic concentration on electrokinetic instability in a cross-shaped microchannel. *Microfluid Nanofluid* **6**, 189–202.

MELCHER, J.R. & SCHWARZ, W.J. 1968 Interfacial relaxation overstability in a tangential electric field. *Phys. Fluids* **11** (12), 2604–2616.

MILANOVA, D., CHAMBERS, R.D., BAHGA, S.S. & SANTIAGO, J.G. 2011 Electrophoretic mobility measurements of fluorescent dyes using on-chip capillary electrophoresis. *Electrophoresis* **32**, 3286–3294.

MILANOVA, D., CHAMBERS, R.D., BAHGA, S.S. & SANTIAGO, J.G. 2012 Effect of PVP on the electroosmotic mobility of wet-etched glass microchannels. *Electrophoresis* **33** (21), 3259–3262.

O'BRIEN, R.W. & HUNTER, R.J. 1981 The electrophoretic mobility of large colloidal particles. *Can. J. Chem.* **59** (13), 1878–1887.

ODDY, M.H., SANTIAGO, J.G. & MIKKELSEN, J.C. 2001 Electrokinetic instability micromixing. *Anal. Chem.* **73** (24), 5822–5832.

POSNER, J.D., PÉREZ, C.L. & SANTIAGO, J.G. 2012 Electric fields yield chaos in microflows. *Proc. Natl Acad. Sci. USA* **109** (36), 14353–14356.

POSNER, J.D. & SANTIAGO, J.G. 2006 Convective instability of electrokinetic flows in a cross-shaped microchannel. *J. Fluid Mech.* **555**, 1–42.

PROBSTEIN, R.F. 2005 *Physicochemical Hydrodynamics: An Introduction*. John Wiley & Sons.

RAMOS, A. 2011 *Electrokinetics and Electrohydrodynamics in Microsystems*, vol. 530. Springer Science & Business Media.

RAMSEY, J.M. 2001 *Micro total analysis systems 2001: proceedings of the MTAS 2001 symposium, held in Monterey, CA, USA, 21–25 October, 2001*. Springer Science & Business Media.

SANTOS, J.J. & STOREY, B.D. 2008 Instability of electro-osmotic channel flow with streamwise conductivity gradients. *Phys. Rev. E* **78** (4), 046316.

SCHNITZER, O. & YARIV, E. 2012 Macroscale description of electrokinetic flows at large zeta potentials: nonlinear surface conduction. *Phys. Rev. E* **86** (2), 021503.

SHARAN, S., GUPTA, P. & BAHGA, S.S. 2017 Mechanism of electrohydrodynamic instability with collinear conductivity gradient and electric field. *Phys. Rev. E* **95**, 023103.

SHULTZ-LOCKYEAR, L.L., COLYER, C.L., FAN, Z.H., ROY, K.I. & HARRISON, D.J. 1999 Effects of injector geometry and sample matrix on injection and sample loading in integrated capillary electrophoresis devices. *Electrophoresis* **20** (3), 529–538.

SIROVICH, L. 1987 Turbulence and the dynamics of coherent structures. I. Coherent structures. *Q. Appl. Maths* **45** (3), 561–571.

SOUNART, T.L. & BAYGENTS, J.C. 2001 Electrically-driven fluid motion in channels with streamwise gradients of the electrical conductivity. *Colloid Surface* A **195** (1–3), 59–75.

WANG, G., YANG, F. & ZHAO, W. 2016 Microelectrokinetic turbulence in microfluidics at low Reynolds number. *Phys. Rev. E* **93** (1), 013106.